

Graphene-Like Carbon Nitride Nanosheets for Improved Photocatalytic Activities

Ping Niu, Lili Zhang, Gang Liu,* and Hui-Ming Cheng

“Graphitic” (g)-C₃N₄ with a layered structure has the potential of forming graphene-like nanosheets with unusual physicochemical properties due to weak van der Waals forces between layers. Herein is shown that g-C₃N₄ nanosheets with a thickness of around 2 nm can be easily obtained by a simple top-down strategy, namely, thermal oxidation etching of bulk g-C₃N₄ in air. Compared to the bulk g-C₃N₄, the highly anisotropic 2D-nanosheets possess a high specific surface area of 306 m² g⁻¹, a larger bandgap (by 0.2 eV), improved electron transport ability along the in-plane direction, and increased lifetime of photoexcited charge carriers because of the quantum confinement effect. As a consequence, the photocatalytic activities of g-C₃N₄ nanosheets have been remarkably improved in terms of •OH radical generation and photocatalytic hydrogen evolution.

1. Introduction

Searching and optimizing highly efficient photocatalysts has attracted worldwide attention due to their potential applications in solar energy conversion.^[1,2] Among various semiconductors investigated,^[3–8] metal-free g-C₃N₄ with a visible-light driven bandgap and proper band edges has emerged as a new class of photocatalyst. Bulk g-C₃N₄, typically prepared by the polycondensation of organic precursors containing both carbon and nitrogen such as cyanamide and dicyandiamide,^[9] exhibits the ability of photocatalytic hydrogen/oxygen evolution from water splitting in the presence of sacrificial reagents and photodegradation of organic pollutants under visible light.^[10] To increase the activity, many strategies such as introducing heteroatoms^[11a–d] or nitrogen vacancy,^[11e] coupling with other semiconductors or dyes,^[12] controlling morphology^[13] have been used, and g-C₃N₄-based photocatalysts have shown encouraging activity improvement.

Nanosheets obtained by the delamination of layered compounds have been recognized as a novel class of nanostructured materials due to their unique structural feature of ultimate two-dimensional anisotropy with extremely small thickness in nanometer and even subnanometer scale.^[14–16] This characteristic often leads to new physicochemical properties in the nanosheets due to the quantum confinement effect. Taking

graphene as an example, it possesses exceptional electronic, thermal, mechanical, optical properties compared to its parent graphite.^[16] As for photocatalysts, nanosheets are extremely advantageous for promoting photocatalysis efficiency. The apparent advantages associated with nanosheets include large specific surface area for providing abundant reactive sites and short bulk diffusion length for reducing the recombination probability of photoexcited charge carriers. The underlying but probably more important advantages are the larger bandgap produced by shifting conduction and valence bands in opposite directions and the changed photophysical behavior of photoexcited

charge carriers, which are caused by the quantum confinement effect. The former can contribute to a stronger redox ability of charge carriers and the latter can play an important role in prolonging the lifetime of charge carriers. The effectiveness of these advantages in improving photocatalytic activity has been primarily demonstrated in several photocatalysts such as ZnO, TiO₂, Ba₅Ta₄O₁₅.^[17–19] Therefore, it is worth anticipating that the nanosheets of g-C₃N₄ will give excellent photocatalytic activity.

Bulk g-C₃N₄ has been historically considered to have a similar layered structure to graphite (The widely claimed “g-C₃N₄” in the literature is actually nonstoichiometric. Here we use “g-C₃N₄” to describe both the bulk material and nanosheets just in order to keep consistent with the general usage.), where there were strong covalent C–N bonds instead of C–C bonds in each layer and weak van der Waals force between layers.^[9] Encouraged by the easy exfoliation of graphite into a monolayer or a few layers of graphene on a large scale by the most widely used Hummers method,^[20] it seems plausible to obtain g-C₃N₄ nanosheets from bulk g-C₃N₄ when one considers the weak *interplanar* interaction between layers in g-C₃N₄. However, the studies on the structure of g-C₃N₄ by Lotsch *et al.* have convincingly suggested that the *planar* cohesion of the so-called g-C₃N₄ obtained from thermal condensation of dicyandiamide is mainly contributed by *hydrogen-bonding* between strands of polymeric melon units with NH/NH₂ groups,^[21] which is definitely different from the planar pure *covalent bonding* cohesion of the graphite. Therefore, the term “graphitic” can not represent the real structure of C₃N₄ at all, and is only historically used. The question then arises whether the hydrogen bonding is strong enough against the oxidation effect exerted by KMnO₄ oxidant used in the Hummers method. Unfortunately, our attempts showed that the Hummers method can only lead to the formation of g-C₃N₄ particles several hundred nanometers

P. Niu, L. L. Zhang, Prof. G. Liu, Prof. H.-M. Cheng
Shenyang National Laboratory for Materials Science
Institute of Metal Research
Chinese Academy of Sciences
72 Wenhua RD, Shenyang 110016, China
E-mail: gangliu@imr.ac.cn



DOI: 10.1002/adfm.201200922

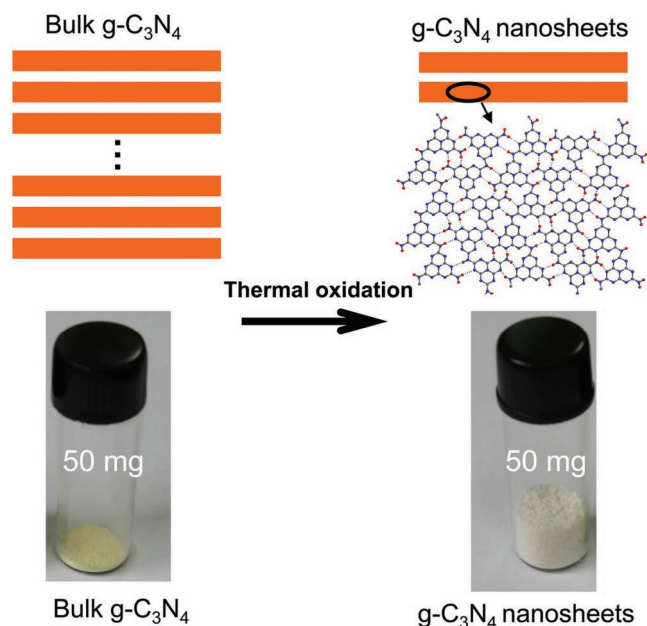


Figure 1. Schematic of the structures of the bulk $g\text{-C}_3\text{N}_4$ and the $g\text{-C}_3\text{N}_4$ nanosheets. Carbon, nitrogen, and hydrogen atoms are respectively indicated by grey, blue and red spheres in the atomic model. A volume comparison of 50 mg powder of bulk $g\text{-C}_3\text{N}_4$ and $g\text{-C}_3\text{N}_4$ nanosheets is given.

thick instead of nanosheets (see Figure S1 of the Supporting Information). What is worse, the planar atomic structure has been seriously destroyed as indicated by the disappearance of the diffraction peak at around 13° in Figure S2 of the Supporting Information, which stems from the lattice planes parallel to the c -axis as depicted in Figure 1.^[21] The failure demonstrates that the existence of medium strong planar hydrogen bonding indeed hampers the effectiveness of the Hummers' method in producing $g\text{-C}_3\text{N}_4$ nanosheets. Clearly, alternative routes must be developed to prepare nanosheets of $g\text{-C}_3\text{N}_4$.

In this work, we developed a simple method to prepare $g\text{-C}_3\text{N}_4$ nanosheets by direct thermal oxidation "etching" process of bulk $g\text{-C}_3\text{N}_4$ in air. The basis of this method is that the hydrogen-bond cohered strands of polymeric melon units in the layers (particularly for short ones), which are not stable enough against (or reactive to) oxidation process in air, will be gradually oxidized away from the bulk material so that the thickness of bulk $g\text{-C}_3\text{N}_4$ will be decreased to the desired nanoscale. The method has the merits of low-cost, easy scale up, and environmental friendliness. The resultant nanosheets were investigated in terms of crystal structure, composition, electronic structure, photophysical behavior and photocatalytic activity. It was found that $g\text{-C}_3\text{N}_4$ nanosheets with a thickness of around 2 nm were obtained and showed much superior photocatalytic activities to the bulk $g\text{-C}_3\text{N}_4$.

2. Results and Discussion

2.1. Morphology and Microstructure of $g\text{-C}_3\text{N}_4$ Nanosheets

The volume of the nanosheets with the same weight is much larger than that of the bulk $g\text{-C}_3\text{N}_4$ (Figure 1), indicating the

fluffy state of the nanosheets. The morphology and microstructure of $g\text{-C}_3\text{N}_4$ nanosheets were investigated with SEM and TEM as shown in Figure 2. Compared to their parent bulk material consisting of solid agglomerates with a size of several micrometers (Figure 2A), the representative nanosheets appear as loose and soft agglomerates with a size of tens of micrometers (Figure 2B). The high-magnification SEM image in Figure 2C confirms that the basic unit of the agglomerates is sheets with a lateral scale ranging from sub-micrometer to several micrometers. Furthermore, the basic sheet tends to bend and its edges are ragged as a result of minimizing the surface-energy of the sheet. The low-magnification TEM image in Figure 2D shows that the nanosheet agglomerates can be dispersed, to some extent. The appearance of a basic sheet in Figure 2E is quite similar to that of graphene. The high-magnification TEM image in Figure 2F demonstrates that the sheet surface is rough. This can be easily understood due to the gradual oxidation decomposition of the strands of polymeric melon units in the layers of bulk $g\text{-C}_3\text{N}_4$ during etching.

To gain the insight into the morphology and thickness of the nanosheets, atomic force microscopy (AFM) images were recorded. The representative AFM image of the nanosheet sample (Figure 3) gives a single $g\text{-C}_3\text{N}_4$ nanosheet deposited on the silicon wafer. The nanosheet is not smooth as demonstrated

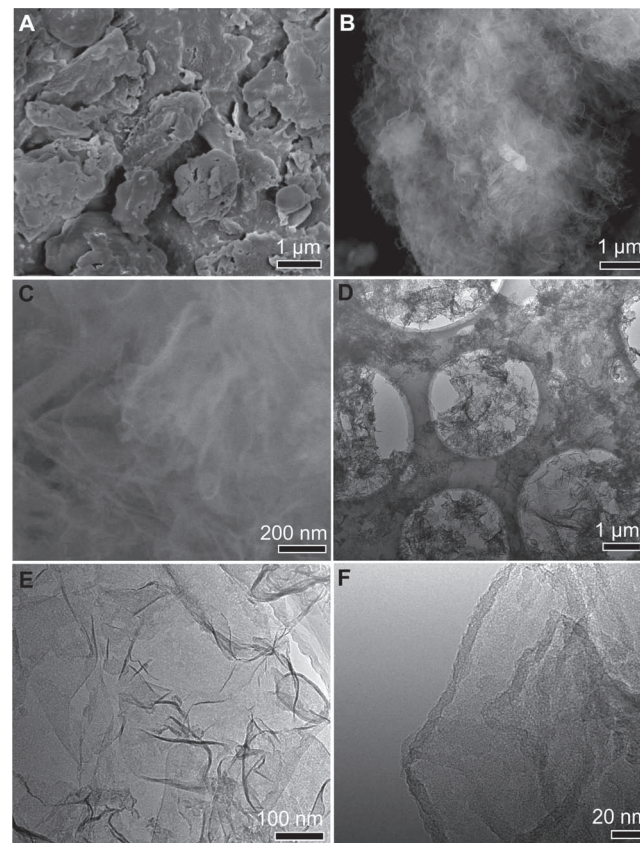


Figure 2. A) SEM image of bulk $g\text{-C}_3\text{N}_4$. Low- (B) and high-magnification (C) SEM images of representative agglomerates of $g\text{-C}_3\text{N}_4$ nanosheets. Low- (D) and high-magnification (E) TEM images of $g\text{-C}_3\text{N}_4$ nanosheets. F) TEM image of the sheet edge area of $g\text{-C}_3\text{N}_4$ nanosheets.

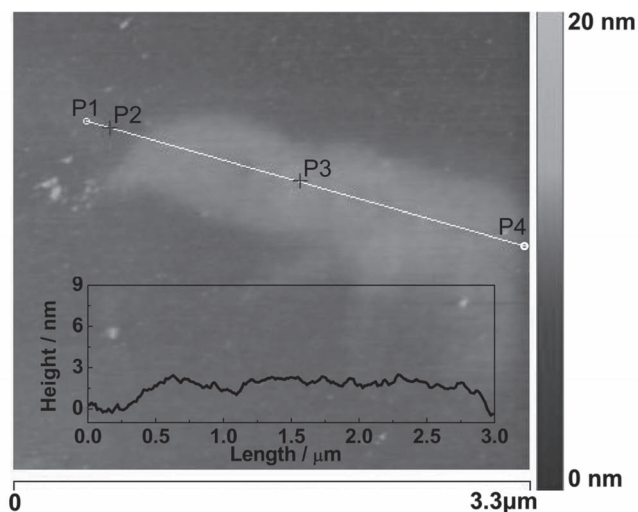


Figure 3. Tapping-mode AFM image of a single $g\text{-C}_3\text{N}_4$ nanosheet deposited on the silicon wafer substrate. The inset is the height curve determined along the line between P1 and P4.

by the TEM image (Figure 2F), which can be further confirmed by the thickness fluctuation determined along the line between Point 1 (P1) and Point 4 (P4) throughout the nanosheet (The inset in Figure 3). The thickness of the nanosheet except its edges ranges from 1.65 to 2.62 nm. For example, the height difference between P2 and P3 is 2.33 nm.

To elucidate the formation process of $g\text{-C}_3\text{N}_4$ nanosheets, we monitored the weight change and morphology evolution of bulk $g\text{-C}_3\text{N}_4$ with the increased thermal oxidation etching time. The weight of the bulk material decreased with the increased etching time (Figure S3, Supporting Information) and only around 6 wt% $g\text{-C}_3\text{N}_4$ was left by 2 h, suggesting the gradual decomposition of solid $g\text{-C}_3\text{N}_4$ into some gaseous products as a result of thermal oxidation etching. **Figure 4** gives the representative SEM images of the $g\text{-C}_3\text{N}_4$ samples collected at different etching times. The thickness of $g\text{-C}_3\text{N}_4$ decreased with the increased etching time. Some sheets were formed after the etching of 90 min. The sample basically appeared as sheets

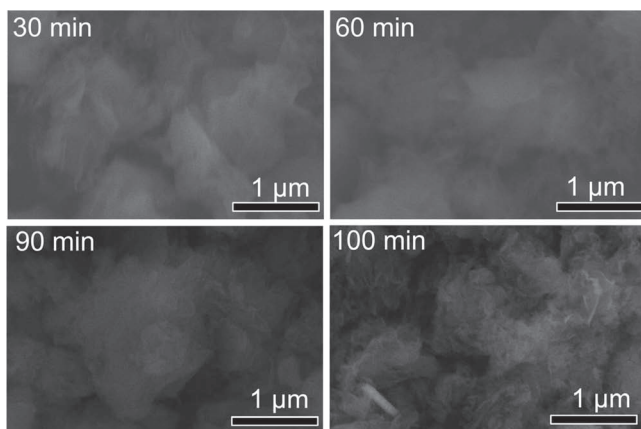


Figure 4. Morphology evolution of bulk $g\text{-C}_3\text{N}_4$ with the increased thermal oxidation etching time at 500 °C in air.

after the etching of 100 min, though the sheet thickness at this stage is not as thin as the nanosheets obtained after the etching of 120 min in Figure 2B. Based on these results, we proposed a layer-by-layer thermal oxidation etching process for the formation of $g\text{-C}_3\text{N}_4$ nanosheets as demonstrated in **Figure 5**.

2.2. The Crystal Structure and Chemical States of $g\text{-C}_3\text{N}_4$ Nanosheets

In the X-ray diffraction patterns shown in **Figure 6A**, the $g\text{-C}_3\text{N}_4$ nanosheets give two consistent peaks with bulk $g\text{-C}_3\text{N}_4$, suggesting that the nanosheets basically have the same crystal structure as their parent bulk $g\text{-C}_3\text{N}_4$. The low-angle reflection peak at 13.1°, stemmed from the lattice planes parallel to the c -axis as depicted in Figure 1,^[21] becomes less pronounced in the nanosheets. It is mainly caused by the simultaneously decreased planar size of the layers during thermal oxidation etching of bulk $g\text{-C}_3\text{N}_4$. A similar phenomenon was also observed in the $g\text{-C}_3\text{N}_4$ nanoparticles.^[22] With respect to the bulk $g\text{-C}_3\text{N}_4$, the peak originated from the periodic stacking of layers in the nanosheets is shifted from 27.34° to 27.67°, indicating a decreased gallery distance between the basic sheets in the nanosheets. It was reported that the single layers in bulk $g\text{-C}_3\text{N}_4$ are potentially undulated, but could be planarized by further heating, resulting in a denser stacking.^[22] In our case, the heating during thermal oxidation process should lead to a denser packing and thus shorten the gallery distance observed.

The crystal structure of the nanosheets can be further confirmed by FTIR spectroscopy. As shown in **Figure 6B**, the characteristic IR spectrum of the nanosheets is similar to that of the bulk material. The sharp peak at around 810 cm^{-1} is originated from heptazine ring system.^[21] The peaks in the region from 900 to 1800 cm^{-1} are attributed to either trigonal C–N(–)C (full condensation) or bridging C–NH–C units,^[21] and these bands become sharper probably due to the more ordered packing of hydrogen-bond cohered long strands of polymeric melon units survived after thermal oxidation etching in the layers of nanosheets. The broad peaks between 3000 and 3600 cm^{-1} are contributed by N–H stretching.

The compositions and chemical states of the nanosheets were investigated by XPS. As shown in **Figure 7**, no obvious binding energy shift of C 1s and N 1s core electrons suggests that the chemical states of both carbon and nitrogen in the nanosheets are the same as in the bulk $g\text{-C}_3\text{N}_4$. According to the percentages of C and N determined by XPS, it is found that the *surface* atomic ratio of C to N has increased from pristine 0.65 for the bulk $g\text{-C}_3\text{N}_4$ to 0.83 for the nanosheets (The *bulk* ratio of C to N increases from pristine 0.66 to 0.68 determined by elemental analysis). Clearly, the nanosheet surface is poor in nitrogen, indicating that the thermal oxidation etching process preferentially proceeds with the oxidation of nitrogen and then loss of carbon. The preferential oxidation of nitrogen atoms during etching can be explained by the fact that the exposed edge nitrogen atoms of polymeric melon units are 50% twofold-coordinated and 50% three-coordinated due to the formed hydrogen bonds, whereas all carbon atoms are threefold-coordinated as indicated in Figure 1.

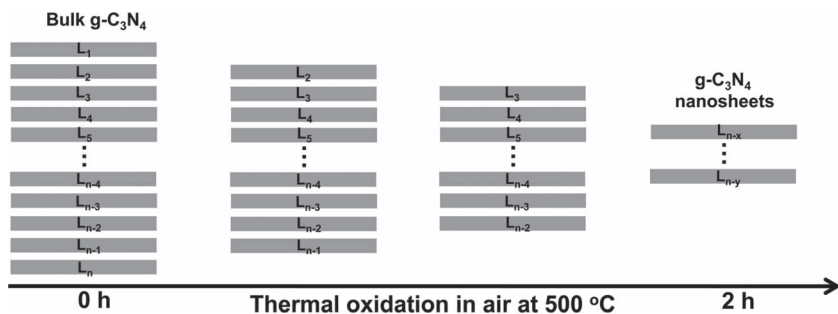


Figure 5. Schematic of the formation process of the $g\text{-C}_3\text{N}_4$ nanosheets by thermal oxidation etching of bulk $g\text{-C}_3\text{N}_4$ at $500\text{ }^\circ\text{C}$ in air.

2.3. Band Structures and Electronic Conductivity of $g\text{-C}_3\text{N}_4$ Nanosheets

As given above, the crystal structure of the nanosheets is basically consistent with that of their parent bulk $g\text{-C}_3\text{N}_4$. We then studied the electronic band structures of the nanosheets by a combined analysis of their optical absorption spectra and fluorescence emission spectra. The UV-visible absorption

spectra in **Figure 8A** show an obvious blue shift of the intrinsic absorption edge in the nanosheets with respect to the bulk $g\text{-C}_3\text{N}_4$. The derived bandgaps from the plots of the $(KM \cdot \text{energy})^n$ ($n = 2$ for the direct bandgap) versus the energy of the light adsorbed are 2.97 and 2.77 eV for the nanosheets and the bulk material. The larger bandgap by 0.2 eV of the nanosheets is further confirmed by the blue shift of the fluorescence emission spectrum by 20 nm in **Figure 8B**. The reason for this larger bandgap is attributed to the well-known quantum confinement effect by shifting the conduction and valence band edges in opposite directions.^[23]

Electronic conduction behavior of the bulk $g\text{-C}_3\text{N}_4$ and the nanosheets was studied by directly measuring I - V curves of single bulk particle and nanosheet. No obvious current can be detected under the applied bias from -10 to 10 V for the single bulk particle (the data is not shown here), indicating the extremely poor electronic conductivity of the bulk $g\text{-C}_3\text{N}_4$. For the single nanosheet a typical semiconducting I - V curve is obtained (**Figure 9**) suggesting the good electron transport along the in-plane direction in the nanosheet. This can be further confirmed by the fact that Pt nanoparticles generated by the reduction of Pt^{4+} with the photoexcited electrons from the nanosheets dominantly locate on the edges of the nanosheets, to be presented in **Figure 12**.

Such obviously different electronic conductivity between the bulk $g\text{-C}_3\text{N}_4$ and nanosheet can be explained by the structure properties of the nanosheets and the bulk material. The layers in the nanosheets, mainly consisting of the large (exactly, long) hydrogen-bond cohered strands of polymeric melon units survived after thermal oxidation etching, can act as good charge carrier transport channels. While the layers in the bulk material, constructing with the strands in various sizes, are actually under the open circuit during I - V measurement due to the role of isolated small strands in blocking electronic transport. The significance of the good charge carrier transport ability along the in-plane direction of the nanosheets is that the photoexcited charge carriers in the nanosheets have a high probability of inducing possible photocatalysis reactions by rapidly reaching the nanosheet edges. Whereas, the photoexcited charge carriers in the bulk $g\text{-C}_3\text{N}_4$ will suffer from serious bulk recombination due to the lack of charge carrier transport channel from bulk to surface. In other words, most of the isolated strands in the layers of the bulk do not contribute to photocatalysis at all. This can partially understand why the activity of bulk $g\text{-C}_3\text{N}_4$ reported is very low, and strongly indicates the necessity of forming $g\text{-C}_3\text{N}_4$ nanosheets in order to obtain high photocatalysis efficiency.

2.4. Photophysical Behaviors of Charge Carriers in $g\text{-C}_3\text{N}_4$ Nanosheets

To understand the photophysical behaviors of photoexcited charge carriers, the time-resolved fluorescence decay spectra of the bulk and nanosheets of $g\text{-C}_3\text{N}_4$ were recorded, as shown in **Figure 10**. The fluorescent intensities of both samples decay

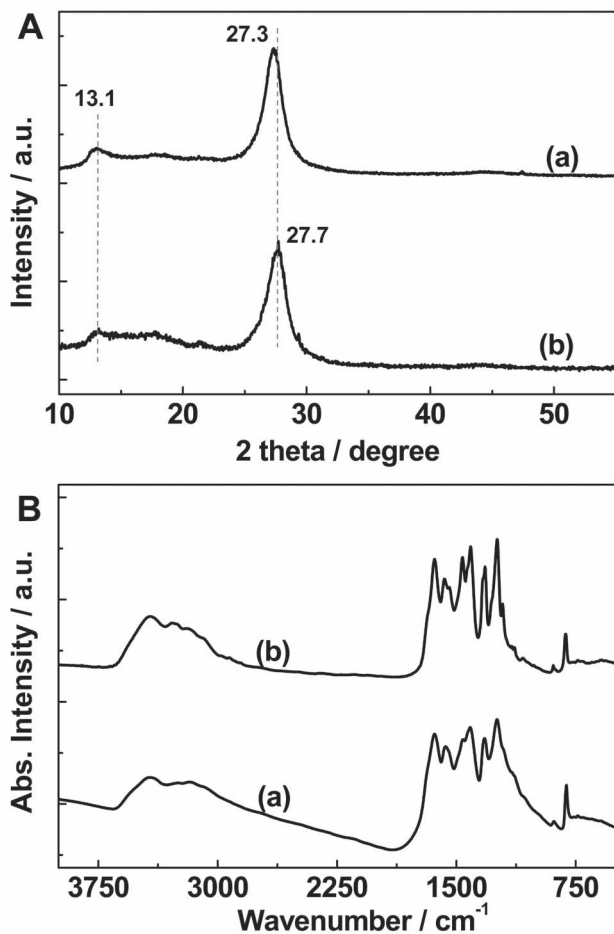


Figure 6. XRD patterns (A), and IR spectra (B) of: a) bulk $g\text{-C}_3\text{N}_4$, and b) $g\text{-C}_3\text{N}_4$ nanosheets.

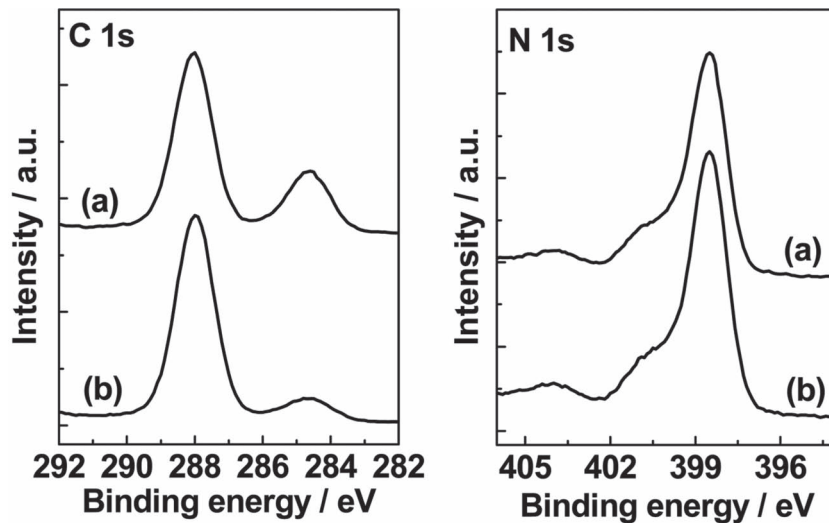


Figure 7. C 1s and N 1s XPS spectra of: a) bulk $g\text{-C}_3\text{N}_4$, and b) $g\text{-C}_3\text{N}_4$ nanosheets. The peak of C 1s at 284.6 eV arises from the adventitious carbon in the samples.

exponentially. Clearly, in contrast to the bulk, the nanosheets show slow decay kinetics. Fitting the decay spectrum shows three radiative lifetimes with different percentages as given in Table 1. In detail, the shortest lifetime of 1.327 ns in the bulk increases up to 1.926 ns in the nanosheets, though its percentage decreases from 27.35% to 19.83%. Both the medium lifetime and percentage of charge carriers increase from 4.153 ns and 43.02% in the bulk to 5.064 ns and 47.21% in the nanosheets. These results mean that the radiative lifetime of around 70% of the charge carriers has been increased by simply decreasing the thickness of the bulk $g\text{-C}_3\text{N}_4$ to the nanosheets, which will play an important role in improving the probability of their involvement in photocatalytic reactions before recombination. Furthermore, the percentage of the charge carriers with the longest lifetime has been increased from 29.63% in the bulk material to 32.96% in the nanosheets at a small cost of shortening the lifetime only by 0.524 ns. It is believed that the increased lifetimes of charge carriers are associated with the improved electron transport and/or electronic band

structure changes induced by quantum confinement effect in the nanosheets.

2.5. Improved Photocatalytic Activities of $g\text{-C}_3\text{N}_4$ Nanosheets

The photocatalytic activities of the $g\text{-C}_3\text{N}_4$ nanosheets were first estimated by detecting the amount of $\bullet\text{OH}$ radicals generated using methods described previously.^[24] It is recognized that $\bullet\text{OH}$ radicals are important active species for decomposing organic molecules.^[25,26] As shown in Figures 11A and B, the nanosheets show a superior ability to the bulk $g\text{-C}_3\text{N}_4$ in generating $\bullet\text{OH}$ radicals under both UV-visible light and only visible light irradiation, though the latter has a wider visible light absorption range. The excellent photocatalytic activity of the $g\text{-C}_3\text{N}_4$ nanosheets is further demonstrated in photocatalytic hydrogen evolution from a water/triethanolamine solution. The average hydrogen evolution rate of the nanosheets under UV-visible light is $170.5 \mu\text{mol h}^{-1}$, which is 5.4 times higher

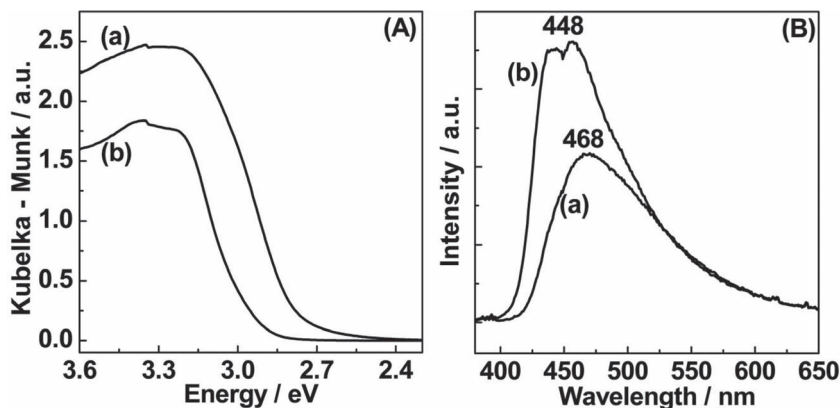


Figure 8. UV-visible absorption spectra (A) and fluorescence emission spectra (B) of: a) bulk $g\text{-C}_3\text{N}_4$ and b) $g\text{-C}_3\text{N}_4$ nanosheets. The wavelength of excitation light for fluorescence emission spectra is 350 nm.

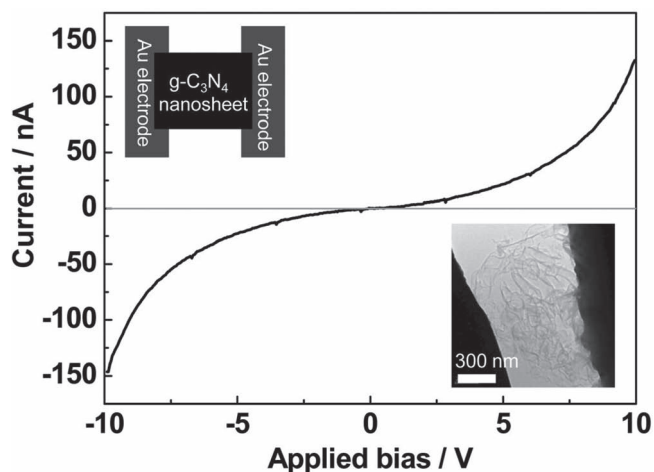


Figure 9. Typical I - V curve of a single $g\text{-C}_3\text{N}_4$ nanosheet. The insets are the schematic (the upper left panel) and the TEM image (the bottom right panel) of the single nanosheet between two Au electrodes.

than that of the bulk counterpart (See Figure 11C). Even under visible light irradiation (Figure 11D), the nanosheets still show an average hydrogen evolution rate 3 times higher than the bulk material. Furthermore, the hydrogen evolution is quite stable, suggesting the stability of the nanosheets as photocatalyst. Both crystal structure and morphology of the nanosheets can be well retained in photocatalysis reaction. As shown in Figure 12, the sample collected after photocatalytic hydrogen evolution reaction for 10 h shows a nearly unchanged nanosheet shape. In addition, the nanoparticles of Pt cocatalyst are well dispersed on the nanosheet edges, demonstrating the potential application of these nanosheets as a substrate for loading other catalysts.

The remarkably improved photocatalytic activities of the nanosheets demonstrated above can be explained as the

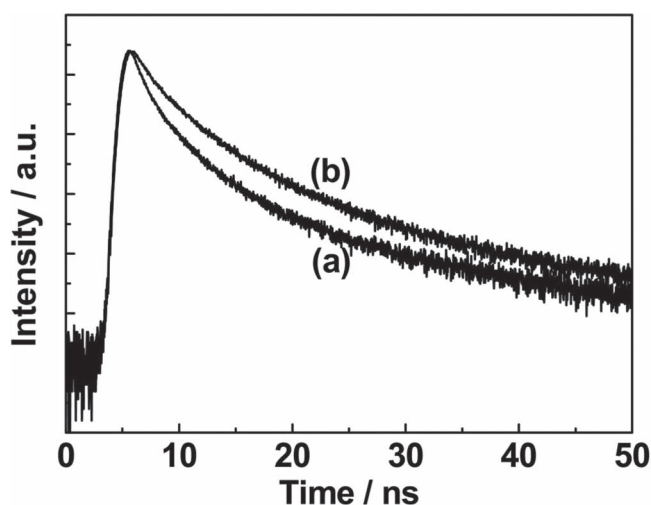


Figure 10. Time-resolved fluorescence decay spectra of a) bulk $g\text{-C}_3\text{N}_4$, and b) $g\text{-C}_3\text{N}_4$ nanosheets monitored at 468 and 448 nm, respectively, by time-correlated single-photon counting. The samples were excited by the incident light of 330 nm from a picosecond pulsed light-emitting diode.

Table 1. The radiative fluorescence lifetimes and their relative percentages of photoexcited charge carriers in the bulk $g\text{-C}_3\text{N}_4$ and $g\text{-C}_3\text{N}_4$ nanosheets.

Sample	τ_1 [ns]-Rel%	τ_2 [ns]-Rel%	τ_3 [ns]-Rel%
Bulk	1.327-27.35	4.153-43.02	16.308-29.63
Nanosheets	1.926-19.83	5.064-47.21	15.784-32.96

synergistic effects of large surface area, increased bandgap, improved electron transport ability and prolonged lifetime of charge carriers. High recombination of charge carriers seriously impairs the overall efficiency of bulk photocatalysts. Due to the small sheet thickness of around 2 nm and improved electron transport ability, the bulk recombination probability of charge carriers can be substantially reduced in the nanosheets. Once charge carriers reach a surface and edge, both surface atomic structure and surface area sensitively affect the surface carrier transfer process. The large surface area can increase the number of possible reactive sites for adsorbing enough reactant molecules and thus promote surface carrier transfer for photocatalytic reactions. The specific surface area of the nanosheets was as high as $306\text{ m}^2\text{g}^{-1}$, whereas the bulk material has a surface area of only $50\text{ m}^2\text{g}^{-1}$ (The N_2 sorption-desorption isotherm in Figure S4 of the Supporting Information). These two properties certainly contribute to the improvement of photocatalytic activities of $g\text{-C}_3\text{N}_4$. Finally but importantly, the intrinsic properties of charge carriers themselves have been changed in the nanosheets as a result of the quantum confinement effect. The increase in the bandgap by 0.2 eV increases the redox ability of charge carriers generated in the nanosheets. The substantial role of a marginally increased bandgap in promoting photocatalytic activities has also been reported from $\text{Cs}_{0.68}\text{Ti}_{1.83}\text{O}_{4-x}\text{N}_x$ and faceted anatase TiO_2 crystals.^[27,28] On the other hand, the lifetimes of charge carriers with a lifetime of shorter than 5 ns have been greatly increased so that the probability of their involvement in photoreactions increases. All these favorable factors co-contribute to the significantly improved photocatalytic activities of the nanosheets in generating $\cdot\text{OH}$ radicals and the photocatalytic evolution of hydrogen under both UV-visible light and visible light.

3. Conclusion

We developed a simple thermal oxidation etching process to prepare nanosheets of $g\text{-C}_3\text{N}_4$ from its parent bulk material. This method has the merits of low-cost, easy scale up, and environmental friendliness. The resultant nanosheets possess not only a large surface area and small sheet thickness but also an increased bandgap, improved electron transport ability along the in-plane direction and prolonged lifetime of charge carriers as a result of the quantum confinement effect. As a result, the nanosheets as photocatalysts show much superior photocatalytic activities to the bulk $g\text{-C}_3\text{N}_4$ under both UV-visible and visible light.

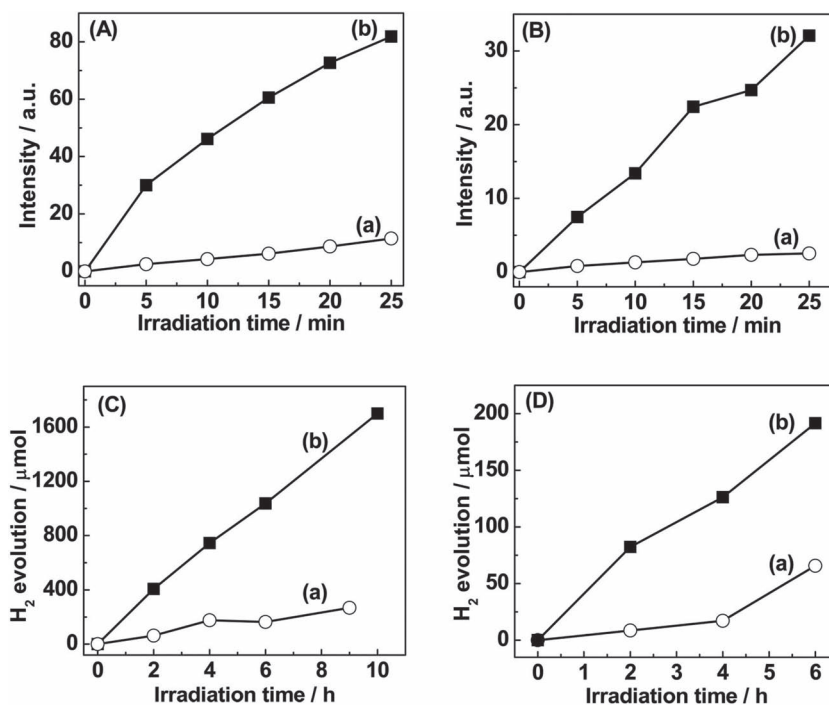


Figure 11. Time-dependent fluorescence signal intensity at 426 nm of 2-hydroxyterephthalic acid generated by reacting terephthalic acid with $\cdot\text{OH}$ radicals in the aqueous suspension of bulk $\text{g-C}_3\text{N}_4$ (a), and $\text{g-C}_3\text{N}_4$ nanosheets (b), under the irradiation of: A) UV-visible light, and B) visible light ($\lambda > 400$ nm). A typical time course of hydrogen evolution from water containing 10 vol% triethanolamine scavenger by Pt-deposited photocatalysts under UV-visible light (C) and visible light irradiation (D): a) bulk $\text{g-C}_3\text{N}_4$, and b) $\text{g-C}_3\text{N}_4$ nanosheets.

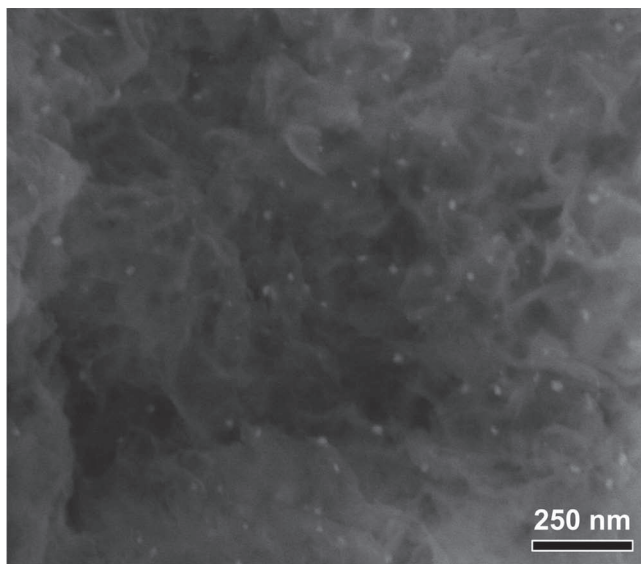


Figure 12. SEM image of $\text{g-C}_3\text{N}_4$ nanosheets collected after photocatalytic hydrogen evolution reaction.

4. Experimental Section

Synthesis of the Bulk $\text{g-C}_3\text{N}_4$ and $\text{g-C}_3\text{N}_4$ Nanosheets: Bulk $\text{g-C}_3\text{N}_4$ powder was synthesized according to a procedure described in a previous paper.^[10a] In detail, dicyandiamide (Aldrich, 99%) was heated

at 550 °C for 4 h in static air with a ramp rate of 2.3 °C/min; the cooling rate was kept at around 1 °C/min. The resultant yellow agglomerates were milled into powder in a mortar. The approximate composition is determined to be $\text{C}_3\text{N}_{4.528}\text{H}_x$ by elemental analysis, which is very close to the reported formula.^[21] The nanosheets were prepared by thermal oxidation etching of the bulk $\text{g-C}_3\text{N}_4$ obtained as above in static air as follows: 400 mg of the bulk $\text{g-C}_3\text{N}_4$ was placed in an open ceramic container and was heated at 500 °C for 2 h with a ramp rate of 5 °C/min. A light yellow powder of $\text{g-C}_3\text{N}_4$ nanosheets was finally obtained with a yield of about 6%. The approximate composition of the nanosheets is determined to be $\text{C}_3\text{N}_{4.425}\text{H}_x$.

Characterization: Elemental analysis was performed on Vario MICRO. X-ray diffraction (XRD) patterns of the samples were recorded on a Rigaku diffractometer using Cu irradiation. Their structure was determined by scanning electron microscopy (SEM) and transmission electron microscopy (TEM) performed on Nova NanoSEM 430 and JEOL 2010 electron microscopes. The Brunauer-Emmett-Teller (BET) specific surface area was determined by nitrogen adsorption-desorption isotherm measurements at 77 K (ASAP 2010). Fourier transform infrared (FTIR) spectra were recorded on a Bruker Tensor 27. Chemical compositions and valence band spectra of the samples were analyzed using X-ray photoelectron spectroscopy (XPS, Thermo Escalab 250, with a monochromatic Al K α X-ray source). All binding energies were referenced to the C 1s peak (284.6 eV) arising from adventitious carbon. The optical absorption spectra of the samples were recorded in a UV-visible spectrophotometer (JASCO V-550). Steady and time-resolved fluorescence emission spectra were recorded at room temperature with a fluorescence spectrophotometer (Edinburgh Instruments, FLSP-920). Electrical conductivity measurements were conducted inside a Tecnai G² F20 TEM equipped with a Nanofactory STM-TEM holder, which integrates a fully functional STM into a TEM. A gold wire of 25 μm with a newly cut edge was used to adhere $\text{g-C}_3\text{N}_4$ powder. The STM gold probe, prepared by electrochemical etching, was controlled by a piezo-manipulator inside

TEM to touch the other end of the individual particle. Then the current voltage characteristic of this system was obtained by applying the bias between the STM probe and $g\text{-C}_3\text{N}_4$.

Photocatalytic Activity Measurements: •OH radical reactions were performed as follows. 5 mg of the photocatalyst was suspended in 80 mL aqueous solution containing 0.01 M NaOH and 3 mM terephthalic acid. Before exposure to light, the suspension was stirred in the dark for 30 min. 5 mL of the solution was then removed every 5 min and centrifuged for fluorescence spectroscopy measurements. During the photoreactions, no oxygen was bubbled into the suspension. A fluorescence spectrophotometer was used to measure the fluorescence signal of the 2-hydroxy terephthalic acid generated. The excitation light wavelength used in recording fluorescence spectra was 320 nm. Water-splitting reactions were carried out in a top-irradiation vessel connected to a glass closed gas circulation system. 50 mg of the photocatalyst powder was dispersed in 300 mL aqueous solution containing 10 vol% triethanolamine scavenger. The deposition of 6 wt% Pt co-catalyst was conducted by directly dissolving H_2PtCl_6 in the above 300 mL reaction solution. The reaction temperature was maintained below 20 °C. The amount of H_2 evolved was determined using a gas chromatography (Agilent 6890). The light source was a 300 W Xe lamp (Beijing Trusttech Co. Ltd, PLS-SXE-300UV). The wavelength of incident light in the visible light photocatalytic reactions was satisfied by using a 400 nm long-pass glass filter.

Supporting Information

Supporting Information is available from the Wiley Online Library or from the author.

Acknowledgements

The authors thank the Major Basic Research Program, Ministry of Science and Technology of China (No. 2009CB220001), NSFC (Nos. 50921004, 51002160, 21090343, 51172243), Solar Energy Initiative of CAS for financial support. GL thanks the IMR SYNLT-S. KeL Research Fellowship.

Received: April 1, 2012

Revised: June 20, 2012

Published online: July 5, 2012

- [1] a) M. R. Hoffmann, S. T. Martin, W. Y. Choi, D. W. Bahnemann, *Chem. Rev.* **1995**, 95, 69; b) A. L. Linsebigler, G. Q. Lu, J. T. Yates Jr., *Chem. Rev.* **1995**, 95, 735; c) H. Tada, T. Kiyonaga, S. Naya, *Chem. Soc. Rev.* **2009**, 38, 1849; d) H. Tada, M. Fujishima, H. Kobayashi, *Chem. Soc. Rev.* **2011**, 40, 4232; e) A. I. Hochbaum, P. D. Yang, *Chem. Rev.* **2010**, 110, 527.
- [2] a) G. Liu, L. Z. Wang, H. G. Yang, H. M. Cheng, G. Q. Lu, *J. Mater. Chem.* **2010**, 20, 831; b) G. Liu, J. C. Yu, G. Q. Lu, H. M. Cheng, *Chem. Commun.* **2011**, 47, 6763.
- [3] a) A. Kudo, Y. Miseki, *Chem. Soc. Rev.* **2009**, 38, 253; b) H. Kato, K. Asakura, A. Kudo, *J. Am. Chem. Soc.* **2003**, 125, 3082.
- [4] Z. G. Zou, J. H. Ye, K. Sayama, H. Arakawa, *Nature* **2001**, 414, 625.
- [5] K. Maeda, K. Teramura, D. L. Lu, T. Takata, N. Saito, Y. Inoue, K. Domen, *Nature* **2006**, 440, 295.
- [6] Z. G. Yi, J. H. Ye, N. Kikugawa, T. Kako, S. X. Ouyang, H. Stuart-Williams, H. Yang, J. Y. Cao, W. J. Luo, Z. S. Li, Y. Liu, R. L. Withers, *Nat. Mater.* **2010**, 9, 559.
- [7] a) X. B. Chen, S. H. Shen, L. J. Guo, S. S. Mao, *Chem. Rev.* **2010**, 110, 6503; b) X. B. Chen, L. Liu, P. Y. Yu, S. S. Mao, *Science* **2011**, 331, 746.
- [8] F. E. Osterloh, *Chem. Mater.* **2008**, 20, 35.
- [9] A. Thomas, A. Fischer, F. Goettmann, M. Antonietti, J. O. Muller, R. Schlögl, J. M. Carlsson, *J. Mater. Chem.* **2008**, 18, 4893.
- [10] a) X. C. Wang, K. Maeda, A. Thomas, K. Takanabe, G. Xin, J. M. Carlsson, K. Domen, M. Antonietti, *Nat. Mater.* **2009**, 8, 76; b) K. Maeda, X. C. Wang, Y. Nishihara, D. Lu, M. Antonietti, K. Domen, *J. Phys. Chem. C* **2009**, 113, 4940; c) X. C. Wang, X. F. Chen, A. Thomas, X. Z. Fu, M. Antonietti, *Adv. Mater.* **2009**, 21, 1609; d) Y. Wang, X. C. Wang, M. Antonietti, *Angew. Chem. Int. Ed.* **2012**, 51, 68.
- [11] a) Y. Wang, J. S. Zhang, X. C. Wang, M. Antonietti, H. R. Li, *Angew. Chem. Int. Ed.* **2010**, 49, 3356; b) G. Liu, P. Niu, C. H. Sun, S. C. Smith, Z. G. Chen, G. Q. Lu, H. M. Cheng, *J. Am. Chem. Soc.* **2010**, 132, 11642; c) Y. J. Zhang, T. Mori, J. H. Ye, M. Antonietti, *J. Am. Chem. Soc.* **2010**, 132, 6294; d) J. S. Zhang, J. H. Sun, K. Maeda, K. Domen, P. Liu, M. Antonietti, X. Z. Fu, X. C. Wang, *Energy Environ. Sci.* **2011**, 4, 675; e) P. Niu, G. Liu, H. M. Cheng, *J. Phys. Chem. C* **2012**, 116, 11013.
- [12] a) Y. J. Zhang, T. Mori, L. Niu, J. H. Ye, *Energy Environ. Sci.* **2011**, 4, 4517; b) Y. J. Zhang, R. Shi, J. Lin, Y. F. Zhu, *Energy Environ. Sci.* **2011**, 4, 2922; c) K. Takanabe, K. Kamata, X. C. Wang, M. Antonietti, J. Kubota, K. Domen, *Phys. Chem. Chem. Phys.* **2010**, 12, 13020; d) S. C. Yan, S. B. Lv, Z. S. Li, Z. G. Zou, *Dalton Trans.* **2010**, 39, 1488; e) X. X. Xu, G. Liu, C. Randorn, J. T. S. Irvine, *Int. J. Hydrogen Energy* **2011**, 36, 13501.
- [13] a) X. C. Wang, K. Maeda, X. F. Chen, K. Takanabe, K. Domen, Y. D. Hou, X. Z. Fu, M. Antonietti, *J. Am. Chem. Soc.* **2009**, 131, 1680; b) X. H. Li, J. S. Zhang, X. F. Chen, A. Fischer, A. Thomas, M. Antonietti, X. C. Wang, *Chem. Mater.* **2011**, 23, 4344.
- [14] a) T. Sasaki, M. Watanabe, H. Hashizume, H. Yamada, H. Nakazawa, *J. Am. Chem. Soc.* **1996**, 118, 8329; b) Y. Omomo, T. Sasaki, L. Z. Wang, M. Watanabe, *J. Am. Chem. Soc.* **2003**, 125, 3568.
- [15] S. Ithurria, M. D. Tessier, B. Mahler, R. P. S. M. Lobo, B. Dubertret, A. L. Efros, *Nat. Mater.* **2011**, 10, 936.
- [16] A. K. Geim, K. S. Novoselov, *Nat. Mater.* **2007**, 6, 183.
- [17] H. B. Lu, S. M. Wang, L. Zhao, J. C. Li, B. H. Dong, Z. X. Xu, *J. Mater. Chem.* **2011**, 21, 4228.
- [18] G. Liu, L. Z. Wang, C. H. Sun, Z. G. Chen, X. X. Yan, L. N. Cheng, H. M. Cheng, G. Q. Lu, *Chem. Commun.* **2009**, 1383.
- [19] T. G. Xu, C. Zhang, X. Shao, K. Wu, Y. F. Zhu, *Adv. Funct. Mater.* **2006**, 16, 1599.
- [20] W. S. Hummers, R. E. Offeman, *J. Am. Chem. Soc.* **1958**, 80, 1339.
- [21] B. V. Lotsch, M. Doblinger, J. Sehnert, L. Seyfarth, J. Senker, O. Oeckler, W. Schnick, *Chem. Eur. J.* **2007**, 13, 4969.
- [22] M. Groenewolt, M. Antonietti, *Adv. Mater.* **2005**, 17, 1789.
- [23] A. P. Alivisatos, *Science* **1996**, 271, 933.
- [24] a) T. Hirakawa, Y. Nosaka, *Langmuir* **2002**, 18, 3247; b) G. Liu, L. Z. Wang, C. H. Sun, X. X. Yan, X. W. Wang, Z. G. Chen, S. C. Smith, H. M. Cheng, G. Q. Lu, *Chem. Mater.* **2009**, 21, 1266.
- [25] A. L. Linsebigler, G. Q. Lu, J. T. Yates, *Chem. Rev.* **1995**, 95, 735.
- [26] M. R. Hoffmann, S. T. Martin, W. Y. Choi, D. W. Bahnemann, *Chem. Rev.* **1995**, 95, 69.
- [27] G. Liu, P. Niu, L. Z. Wang, G. Q. Lu, H. M. Cheng, *Catal. Sci. Technol.* **2011**, 1, 222.
- [28] a) G. Liu, C. H. Sun, H. G. Yang, S. C. Smith, L. Z. Wang, G. Q. Lu, H. M. Cheng, *Chem. Commun.* **2010**, 46, 755; b) J. Pan, G. Liu, G. Q. Lu, H. M. Cheng, *Angew. Chem. Int. Ed.* **2011**, 50, 2133.